A MEASUREMENT OF SEMI INCLUSIVE DEEP INELASTIC SCATTERING PION ASYMMETRIES TO TEST INDEPENDENT FRAGMENTATION

T. Didberidze and T. Forest

Department of Physics, Idaho State University, Pocatello, ID 83201, USA

December 17, 2012

Abstract

Semi-inclusive deep inelastic scattering (SIDIS) experiments may be used to identify the flavor of the quark that participates in the scattering process. Semi-inclusive scattering is defined as an electron scattering experiment in which the scattered electron and one hadron are detected in the final state. Experiments at Jefferson Lab have used longitudinally polarized electron beams to probe longitudinally polarized Hydrogen ($^{15}NH_3$) and Deuterium ($^{15}ND_3$) targets to investigate the quark's contribution to the properties of a nucleon. This work reports a measurement of SIDIS pion asymmetries using the CEBAF Large Acceptance Spectrometer (CLAS) at Thomas Jefferson National Laboratory. The incident electron's energy was 4.2 GeV and covered a kinematic region where the struck quark carries at least 30% of the nucleons total momentum ($x_B \geq 0.3$). The electrons scatter mostly from valence quarks in this kinematic region allowing measurements which are less sensitive to the ocean of quark-antiquark pairs that are also inside a nucleon.

Table of Contents

List of Figures

List of Tables

Chapter 1

Data Analysis

This chapter describes the techniques used to analyze the data collected during the EG1b experiment and calculate semi-inclusive cross sections for the following reactions: $\overrightarrow{e}^{-}\overrightarrow{N} \rightarrow e^{-}\pi^{+}X$ and $\overrightarrow{e}^{-}\overrightarrow{N} \rightarrow e^{-}\pi^{-}X$ using NH_3 and ND_3 polarized targets respectively. The goal of this work is to measure charged pion asymmetries defined according to the incident electron helicity and the target polarization. The measured asymmetries may be used to determine if the fragmentation function is independent of the observed final state hadron fractional energy (z) [1]. The quantity ($\Delta R_{np}^{\pi^+ + \pi^-}$) is defined in terms of the ratio of the difference of polarized semi-inclusive deep inelastic scattering cross sections for proton and neutron targets to unpolarized cross sections:

$$\Delta R_{np}^{\pi^+ + \pi^-} = \frac{\Delta\sigma_p^{\pi^+ + \pi^-} - \Delta\sigma_n^{\pi^+ + \pi^-}}{\sigma_p^{\pi^+ + \pi^-} - \sigma_n^{\pi^+ + \pi^-}}. \tag{1.1}$$

A measure of ΔR can be used to test for independent fragmentation when it is compared to inclusive structure functions.

1.0.1 The CLAS Data Selection

The data files from the EG1b experiment chosen for this analysis are listed in Table 1.1. During the experiment, 2.2 GeV, 4.2 GeV and 5.7 GeV longitudinally

polarized electron beams were used to probe the polarized frozen ammonia NH_3 and ND_3 targets. This work will discuss the analysis of the 4.2 GeV energy electron beam data set as this energy provided the most statistics. The collected data have been tested by applying restrictions discussed later in this chapter.

Run Set	Target Type	Torus Current(A)	Target Polarization	HWP
28100 - 28102	ND_3	+2250	-0.18	+1
28106 - 28115	ND_3	+2250	-0.18	-1
28145 - 28158	ND_3	+2250	-0.20	+1
28166 - 28190	ND_3	+2250	+0.30	+1
28205 - 28217	NH_3	+2250	+0.75	+1
28222 - 28236	NH_3	+2250	-0.68	+1
28242 - 28256	NH_3	+2250	-0.70	-1
28260 - 28275	NH_3	+2250	+0.69	-1
28287 - 28302	ND_3	-2250	+0.28	+1
28306 - 28322	ND_3	-2250	-0.12	+1
28375 - 28399	ND_3	-2250	+0.25	-1
28407 - 28417	NH_3	-2250	+0.73	-1
28456 - 28479	NH_3	-2250	-0.69	+1

Table 1.1: EG1b runs analyzed for this work.

1.1 Particle Identification

Additional tests were performed on the electron and a pion candidates reconstructed using the standard CLAS software package on the raw data collected during the EG1b experiment. Electrons are identified by matching the charged particle hits in the Cherenkov counter, electromagnetic calorimeter, and Time of Flight system. Geometrical and timing cuts are applied to improve electron identification. In addition, cuts are applied on the energy deposited by the

particle into the calorimeter and the number of photoelectrons produced in the Cherenkov counter. Charged pions are identified by matching the hits in the drift chamber and ToF counter, along with a Cherenkov cut requiring that the number of photons for pions be less than two.

1.1.1 Electron Identification

The CLAS trigger system required the particle to deposit energy in the electromagnetic calorimeter and illuminate the Cherenkov counter within a 150 ns time window (Figure 1.1). Unfortunately, this trigger suffers from a background of high energy negative pions that may be misidentified as electrons. The pion contamination of the electron sample is reduced using cuts on the energy deposited in the electromagnetic calorimeter and the momentum measured in the track reconstruction for the known magnetic field. The energy deposition mechanism for the pions and electrons in the electromagnetic calorimeter is different. The total energy deposited by the electrons in the EC is proportional to their kinetic energy, whereas pions are minimum ionizing particles and the energy deposition is independent of their momentum (Figure 1.2). The pion background is further suppressed using geometrical and time matching between the Cherenkov counter hit and the measured track in the drift chamber.

EC CUTS

The CLAS electromagnetic calorimeter was used to reduce the misidentification of electron and negative pion candidates. The electromagnetic calorimeter contains thirteen layers of lead-scintillator sandwiches composed of $\sim$ 2 mm thick

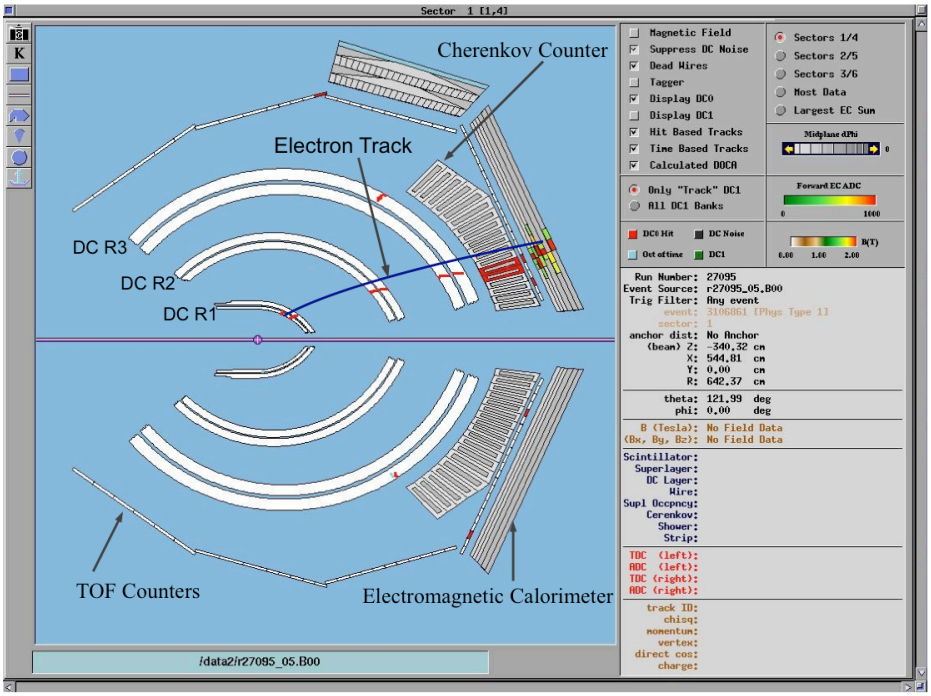

Fig. 1.1: Example of electron passing through the drift chambers and creating the signal in the Cherenkov counter and electromagnetic calorimeter. Electron track is highlighted by the blue line (Run number 27095, Torus Current +2250 (inbending)).

lead and 10 mm thick scintillator. Each set of thirteen layers are subdivided into five inner and eight outer layers that are named the inner and outer calorimeter respectively. Electrons interact with the calorimeter producing electromagnetic showers that release energy into the calorimeter. The deposited energy is proportional to the momentum of the electrons. Figure 1.3 shows the correlation of the inner and outer calorimeter electron candidate's energy measured by the calorimeter and divided by the particles momentum reconstructed by the drift chamber. As shown in the Figure 1.3, there is an island near $E/p = 0.2$, which contains most of the electron candidates as well as some regions below 0.2 which will be argued to be negative pions misidentified as electrons.

Pions entering the calorimeter are typically minimum ionizing particles, loos-

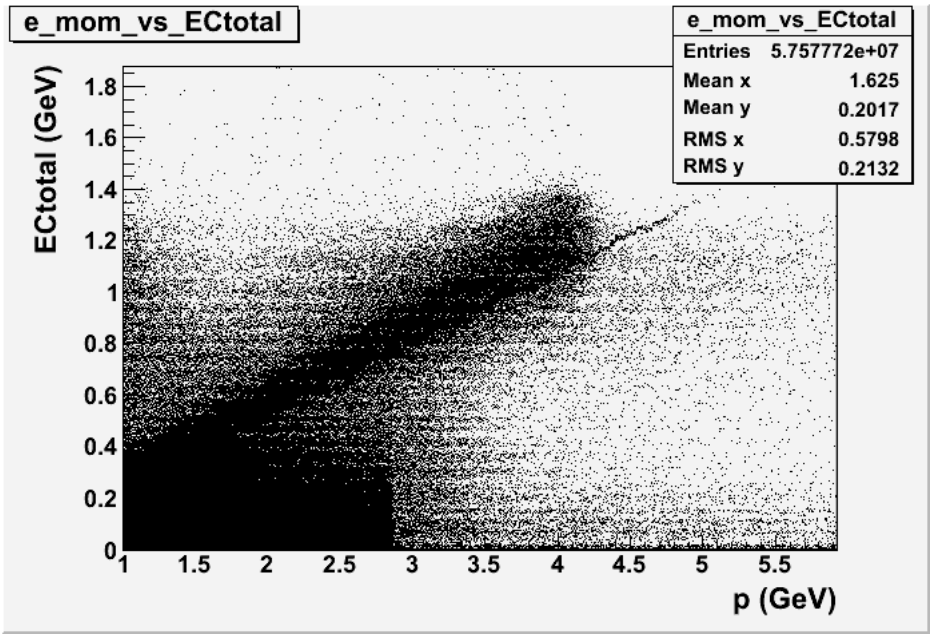

Fig. 1.2: Momentum versus ECtotal.

ing little of their incident energy in the calorimeter at a rate of 2 MeV $g^{-1}cm^2$. Electrons, on the other hand, deposit a larger fraction of their momentum into the calorimeter. As a result, the energy deposited into the electromagnetic calorimeter is different for electrons and pions. Pions loose about 0.08 GeV of energy traversing the calorimeter independent their momentum thereby producing the constant signal in the calorimeter around 0.08 GeV. In order to reduce misidentified pions from the electron sample, the following cut has been applied:

$$EC_{inner} > 0.08 \times p, \tag{1.2}$$

where p represents particle momentum and EC_{inner} the inner part of the calorimeter.

Since the energy loss of pions is related to the calorimeter thickness, a correla-

tion can be established between the energy deposited into the inner and outer layers of the calorimeter:

$$\frac{EC_{tot}}{EC_{inner}} = \frac{13}{5}, \tag{1.3}$$

which gives the following cut for the energy deposition into the outer layer of the calorimeter:

$$EC_{tot} > 0.2 \times p. \tag{1.4}$$

Cherenkov Counter Cut

The Cherenkov counter has been used to further reduce the negatively charged pion background in the reconstructed electron sample. When the velocity of a charged particle is greater than the local phase velocity of light or when it enters a medium with different optical properties, the charged particle will emit photons. Cherenkov light is emitted at the critical angle θ_c representing the angle of Cherenkov radiation relative to the particle's direction. It can be shown that the cosine of the Cherenkov radiation angle is inversely proportional to the velocity of the charged particle

$$\cos\theta_c = \frac{1}{n\beta}, \tag{1.5}$$

where βc is the particle's velocity and n the index of refraction of the medium. The charged particle in time t travels a distance βct, while the electromagnetic waves travel $\frac{c}{n}t$. For a medium with given index of refraction n, there is a threshold velocity $\beta_{thr} = \frac{1}{n}$, below which no radiation is emitted. This process may be used to distinguish between the highly relativistic electrons and the less

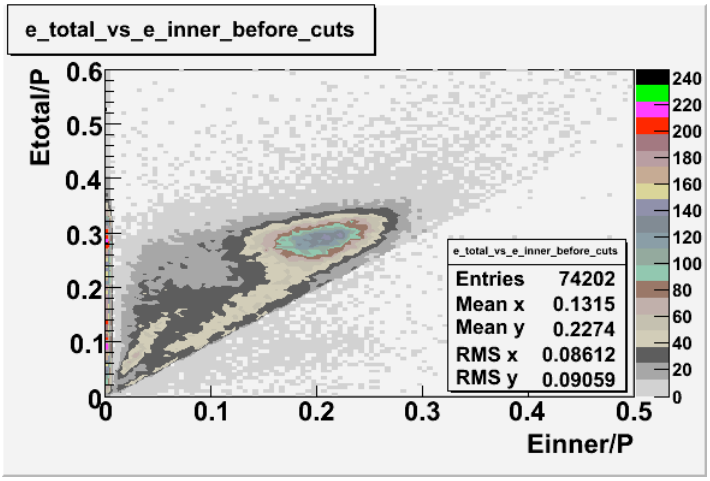

(a) Before cuts.

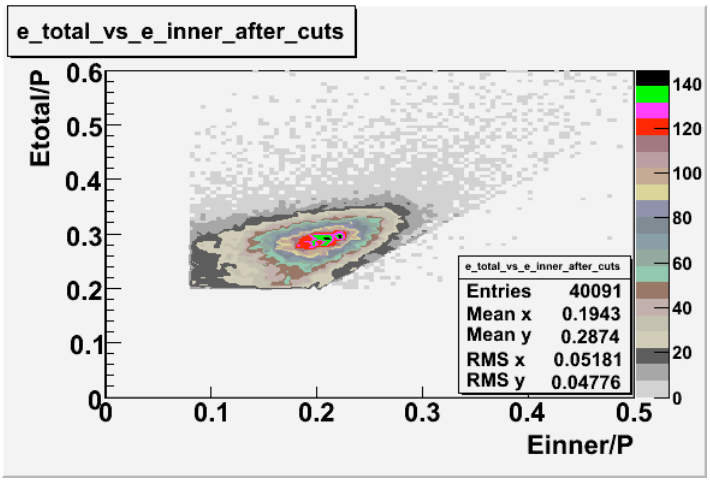

(b) After cuts.

Fig. 1.3: EC_{inner}/p versus EC_{tot}/p before and after EC cuts ($EC_{tot} > 0.2p$ and $EC_{inner} > 0.08p$). After applying EC cuts about 46% of the events have been removed from the electron sample.

relativistic pions based on the number of photons produced. The number of photons produced per unit path length of a particle with charge Ze and per unit energy interval of the photons is proportional to the sine of the Cherenkov angle [2]

$$\frac{d^2N}{dEdx} = \frac{\alpha z^2}{\hbar c}\sin^2\theta_c = \frac{\alpha z^2}{\hbar c}\left[1 - \frac{1}{\beta^2 n^2(E)}\right] \tag{1.6}$$

$$\frac{d^2N}{d\lambda dx} = \frac{2\pi\alpha z^2}{\lambda^2}[1 - \frac{1}{\beta^2 n^2(\lambda)}] \tag{1.7}$$

$$\beta = \frac{v}{c} = \frac{pc}{\sqrt{(pc)^2 + (mc^2)^2}}. \tag{1.8}$$

Taylor expanding Eq. 1.6 and keeping only the first two terms we get following

$$\frac{d^2N}{dEdx} = \frac{\alpha z^2}{\hbar c}\sin^2\theta_c = \frac{\alpha z^2}{\hbar c}[\beta^2 n^2(E) - 1]. \tag{1.9}$$

The gas used in the CLAS Cerenkov counter is perfluorobutane C_4F_{10} with index of refraction equal to 1.00153. The number of photoelectrons emitted by electrons is about thirteen. On the other hand, calculations show that the number of photons produced by the negatively charged pions in the Cherenkov detector is approximately 2. The theoretical results of the number of photons produced by the electrons and pions when passing through the Cherenkov counter are shown on Figure 1.4.

The distribution of the number of photoelectrons measured in the Cherenkov detector and the energy deposition dependence on number of photoelectrons are shown on Figure 1.5 and Figure 1.6. One can see that a single photoelectron peak is caused by misidentifying pions as electrons.

Geometric and Timing cuts

Negative pions may be produced when the lepton scatters at a polar angle close to zero and is not observed by the detector. In order to reduce the electron sample contamination due to those pions, geometrical cuts on the location of the

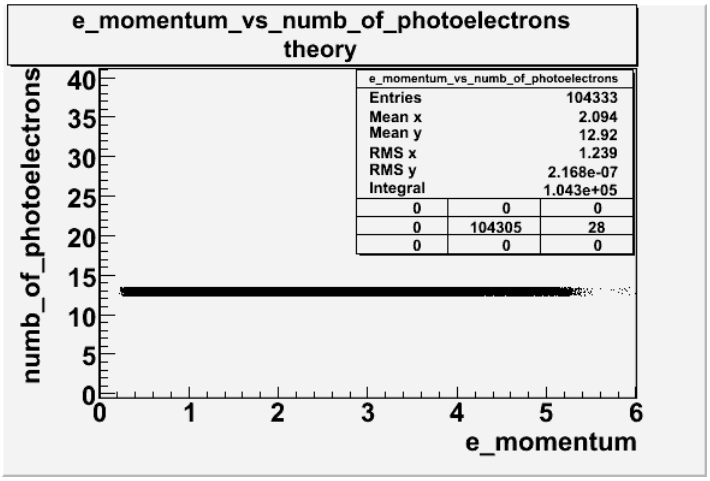

(a) For electrons.

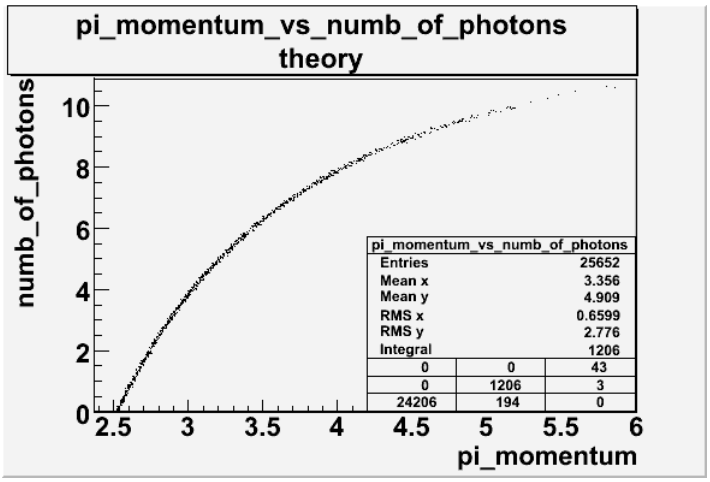

(b) For pions.

Fig. 1.4: Theoretical Calculation of the Number of Photoelectrons for electrons and pions.

particle at the entrance to the Cherenkov detector and time matching cuts have been developed by Osipenko, so called OSI cuts [3]. For each CLAS Cherenkov detector segment the following cut has been applied

$$|\theta_p - \theta_p{}^{center} - \theta_p{}^{offset}| < 3\sigma_p, \tag{1.10}$$

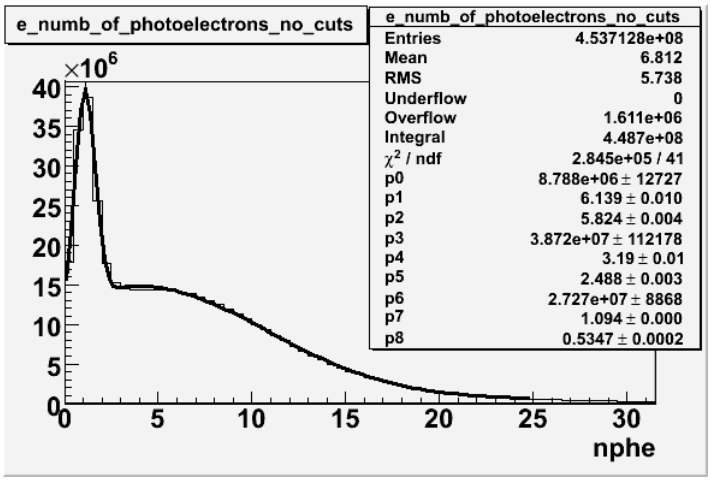

Fig. 1.5: The number of photoelectrons without cuts.

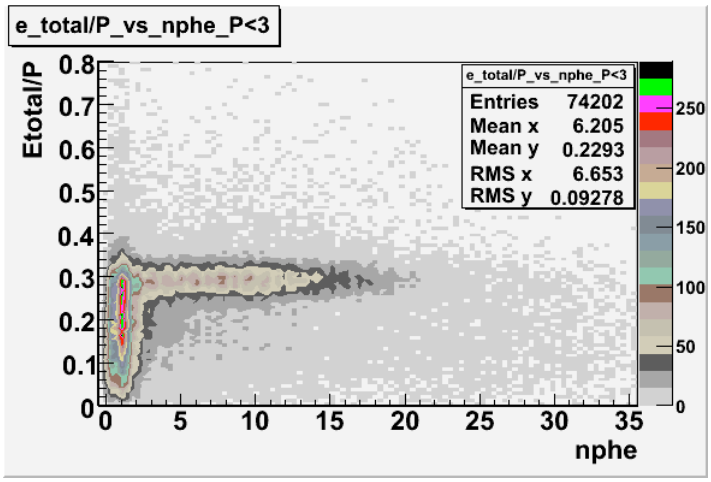

Fig. 1.6: The total energy deposited into the Calorimeter versus the Number of Photoelectrons.

where θ_p represents the measured polar angle with respect to a projectile plane for each electron event. The Cherenkov counter's projective plane is an imaginary plane behind the Cherenkov detector where Cherenkov radiation would have arrived if it had moved the same distance from emission point to the PMT, without reflections in the mirror system. ${\theta_p}^{center}$ is the polar angle from the CLAS detector center to the image of Cherenkov counter segment center

and ${\theta_p}^{offset}$ is the shift in the segment center position. In addition to geometrical cuts, timing cuts have been applied to match the time between a Cherenkov counter hit and time of flight system.

The pion contamination in an electron sample was estimated by fitting the number of photoelectron distribution using two Gaussian distributions convoluted with a Landau distribution [4]:

$$N_{pe} = p_0 e^{-0.5\left(\frac{x-p_1}{p_2}\right)^2} + p4\frac{1}{1-\left(\frac{x-p5}{p6}\right)} + p_6 e^{-0.5\left(\frac{x-p_7}{p_8}\right)^2}. \tag{1.11}$$

The fits in Figure 1.7.(a) suggest that the pion contamination in the electron sample is $9.63\% \pm 0.01\%$ before applying the OSI cuts and after the OSI cuts the contamination is about $4.029\% \pm 0.003\%$ (Figure 1.7.(b)).

1.1.2 Pion Identification

Charged pions are identified using a coincidence hit in the drift chamber and Time-of-Flight (ToF) counter. Pions are separated from the other charged particles by looking at the particle momentum versus the β distribution. The particle velocity, $\beta = \frac{v}{c}$, is calculated from the difference of the RF time and the time-of-flight measurement in the ToF system with the path length from the vertex to the ToF counters. The mass of the charged particle can be identified by combining the particle's β with the particle momentum obtained from the track measured by the drift chamber in the known magnetic field. The particle

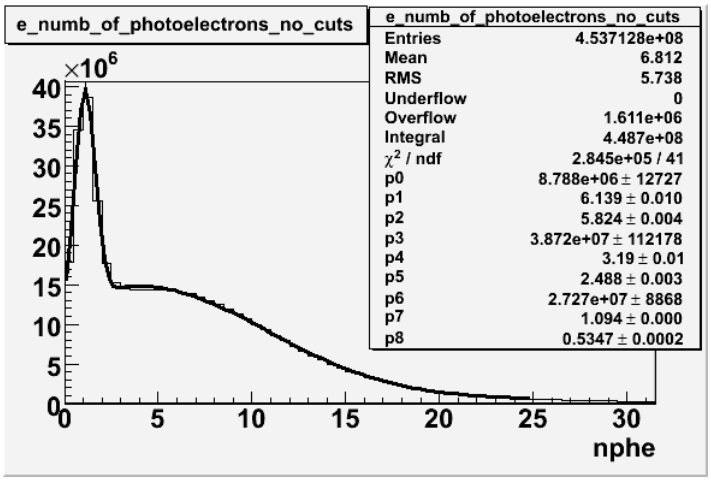

(a) Before Cuts.

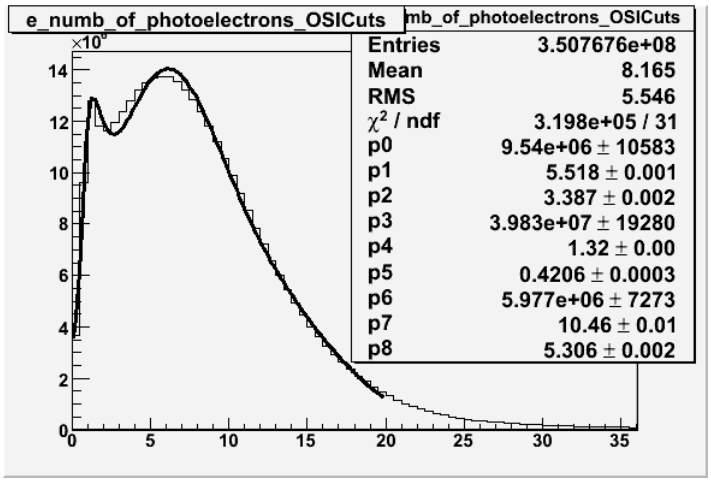

(b) After OSI Cuts.

Fig. 1.7: The number of photoelectrons before and after geometrical and time matching cuts.

mass in a magnetic field is given as

$$p = \frac{m\beta}{\sqrt{1-\beta^2}} \tag{1.12}$$

$$m = p\sqrt{(\beta^2 - 1)} \tag{1.13}$$

$$\beta = \frac{L_{path}}{t_{flight}}, \tag{1.14}$$

where m is the mass of the charged particle, β its velocity, p particle momentum, L_{path} the path length from the vertex to scintillators and t_{flight} the time of flight from the interaction vertex to the ToF system.

Using the above information (particle momentum from the drift chambers and the timing information from the ToF system), the mass squared of the charged particle was calculated and is shown on Figure 1.9. The pion mass band is around ~ 0. To isolate charged pions from the rest of the particles, a 3σ cut on the momentum versus β distribution has been applied [5].

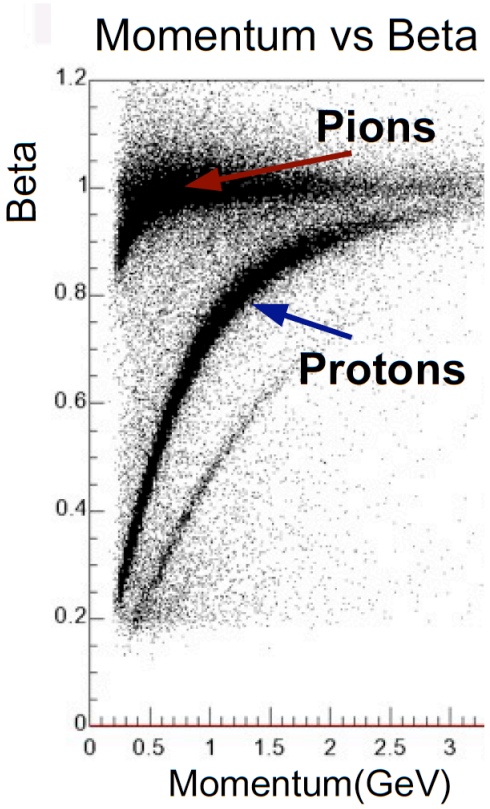

Fig. 1.8: The charged particle momentum versus β distribution. The pion and proton bands are clearly separated.

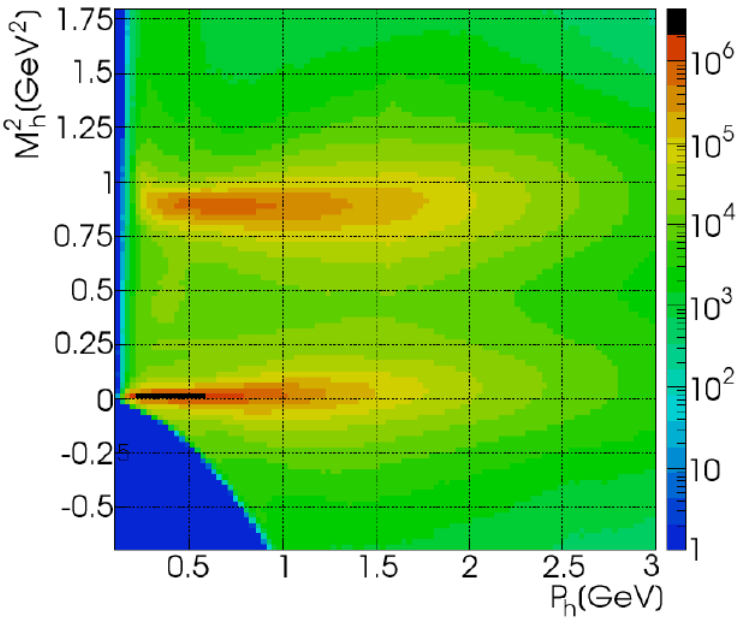

Fig. 1.9: The charged particle momentum versus mass squared distribution for the $\overrightarrow{e}p \rightarrow \overrightarrow{e}'\pi^+ n$ electroproduction process. The bands around 0 and 1 represent pions and protons respectively [5].

In addition to the charged particle velocity (β), the fiducial volume cuts have been applied for the charged pion identification. Since the drift chambers and scintillators are used for pion detection, the polar angle range where pions are detected is much larger than for electrons. For the EG1b experiment, pions were detected from 8° to 180° [5]. The pion identification code has been developed by Joshua Pierce [6].

1.2 Event Reconstruction Efficiency

The goal of this work is to measure the semi-inclusive asymmetry when an electron and a pion are detected in the final state. For this analysis, pions of opposite charge will be observed using the same scintillator paddles by flipping

the CLAS torus magnetic field direction. Although the pions will be detected by the same detector elements, the electrons will intersect different detector elements. As a result, the electron reconstruction efficiency was evaluated in terms of the electron rate observed in two different scintillator paddles detecting the same electron kinematics.

1.2.1 Inclusive Electron Event Reconstruction Efficiency

The electron reconstruction efficiency for individual scintillator detectors using the 4.2 GeV EG1b data is investigated below. Only the electron is detected in the final state (inclusive case). The pion contamination in the electron sample was removed by applying the cuts described above. The electron paddle numbers 10 (B<0) and 5 (B>0) were chosen respectively, because they contained the most electron events in a first pass semi-inclusive pion analysis of the data set. The electron kinematics (momentum, scattering angle and invariant mass) for these scintillators is shown on Figure 1.10.

Ratios of the inclusive electron rate, normalized using the gated Faraday cup, detected in scintillator paddles # 5 and # 10 were measured. The two ratios are constructed to quantify the CLAS detector's ability to reconstruct electrons in scintillator paddle #5 using a positive Torus polarity and scintillator #10 using the negative Torus polarity.

$$\frac{ND_3, B > 0, PaddleNumber^{e^-} = 5}{ND_3, B < 0, PaddleNumber^{e^-} = 10} = 1.57 \pm 0.16 \tag{1.15}$$

$$\frac{NH_3, B > 0, PaddleNumber^{e^-} = 5}{NH_3, B < 0, PaddleNumber^{e^-} = 10} = 1.76 \pm 0.17. \tag{1.16}$$

Notice the above ratios are statistically the same. The semi-inclusive analysis to be performed in this work will be taking ratios using an ND_3 and NH_3 target. Below is the observed ratio comparing the inclusive electrons observed in scintillator #5 for a positive torus polarity and an ND_3 target to the electrons observed in scintillator #10 when the torus polarity is negative and the target is NH_3.

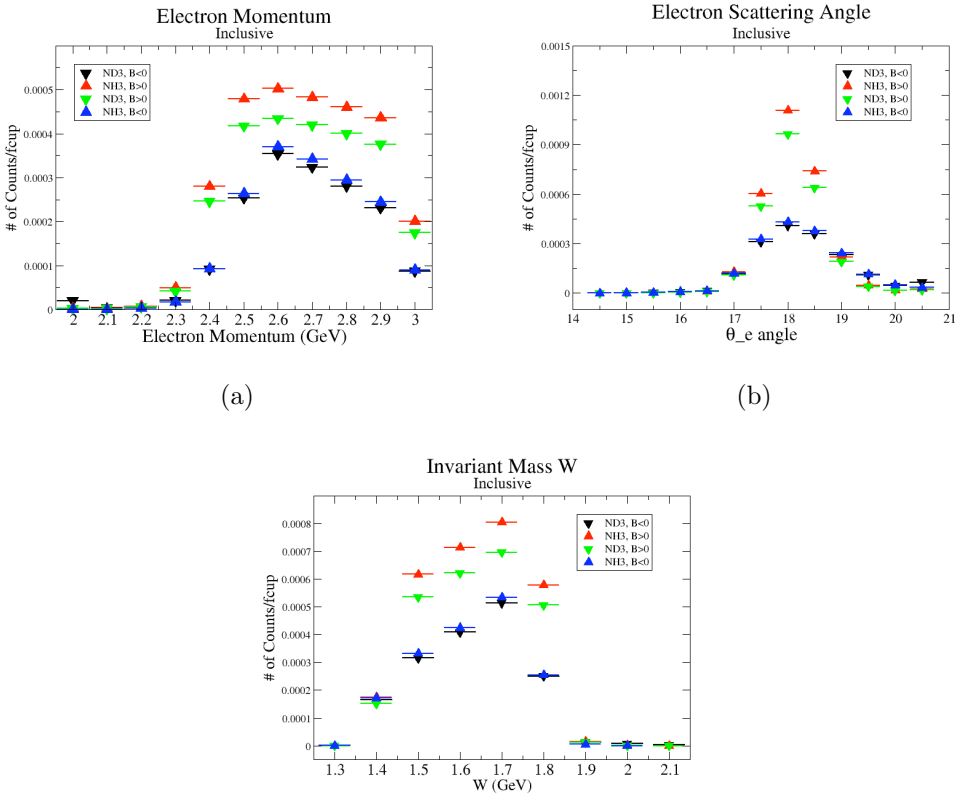

(a) (b)

(c)

Fig. 1.10: Electron Kinematics. (a) Electron Momentum((NH_3,B>0), (NH_3,B<0), (ND_3,B>0) and (ND_3,B<0)), (b) Electron Scattering Angle θ ((NH_3,B>0), (NH_3,B<0), (ND_3,B>0) and (ND_3,B<0)) and (c) W Invariant mass((NH_3,B>0), (NH_3,B<0), (ND_3,B>0) and (ND_3,B<0))

$$\frac{ND_3, B > 0, PaddleNumber^{e^-} = 5}{NH_3, B < 0, PaddleNumber^{e^-} = 10} = 1.55 \pm 0.15. \tag{1.17}$$

The above ratios, which have been observed to be ammonia target independent, indicate a difference in an electron detector efficiency when the torus polarity is flipped. An electron detection efficiency "correction coefficient" is defined in terms of the above ratio and measured to be $\frac{ND_3,B>0,E_{PaddleNumber=5}}{NH_3,B<0,E_{PaddleNumber=10}} = 0.645$ and $\frac{ND_3,B<0,E_{PaddleNumber=10}}{NH_3,B>0,E_{PaddleNumber=5}} = 1.82$. The impact of these corrections on the data is illustrated in the next section.

1.2.2 Exclusive and Semi-Inclusive Event Reconstruction Efficiencies

After determining the electron reconstruction efficiency for the selected paddle numbers, the measured single pion electroproduction rate was compared to the MAID 2007 unitary model that has been developed using the world data of pion photo and electro-production to determine the impact of using the above "correction coefficient". The model is well adopted for predictions of the observables for pion production, like five fold cross section, total cross section, etc.

The MAID 2007 model has predictions of the total cross section for the following two cases that are related to our work:

$$\gamma^* + \text{proton}(\text{NH}_3) \rightarrow \pi^+ + \text{neutron} \tag{1.18}$$

$$\gamma^* + \text{neutron}(\text{ND}_3) \rightarrow \pi^- + \text{proton}. \tag{1.19}$$

The ratio of the pions detected in the scintillator paddles, located between the

Cherenkov counter and electromagnetic calorimeter, is shown in Figure 1.11. The ratios were taken for four different cases. The intrinsic assumption is that, for the inbending case, positive pions and for the outbending case negative pions have the same trajectories with the same kinematics. In addition, negatively charged pions in the inbending field and positively charged pions in the outbending fields are detected by the same detector elements.

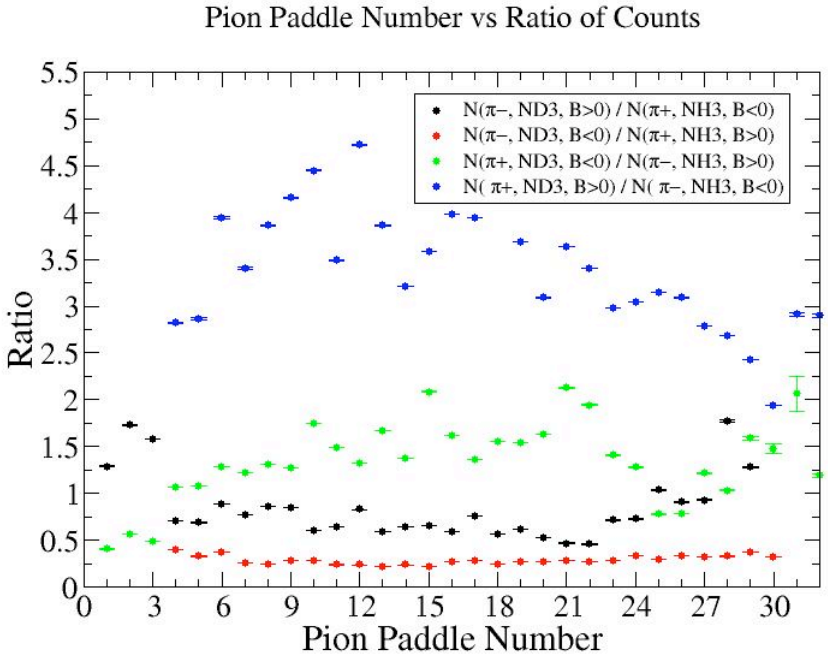

Fig. 1.11: Pion paddle number versus Ratio for Semi-Inclusive case.

Using MAID 2007, the total cross section was calculated for the following invariant mass and four momentum transferred square values: 1.7 GeV < W<1.8 GeV and Q^2=1.1 GeV^2 [7].

$$\sigma = \sigma_T + \epsilon\sigma_L + \sqrt{2\epsilon(1+\epsilon)}\sigma_{LT}\cos\phi_\pi{}^{CM} + + \epsilon\sigma_{TT}\cos 2\phi_\pi{}^{CM} + h\sqrt{2\epsilon(1-\epsilon)}\sigma_{LT'}\sin\phi_\pi{}^{CM}, \tag{1.20}$$

where ${\phi_\pi}^{CM}$ is the pion azimuthal angle in the CM frame, $\epsilon = (1 + 2(1 + \frac{\nu^2}{Q^2}) \tan^2 \frac{\theta_e}{2})^{-1}$ is the virtual photon polarization, $\nu = E_i - E_f$ the energy difference of the initial and final state electron, $Q^2 = 4E_iE_f \sin^2 \frac{\theta_e}{2}$ the four momentum transferred squared, θ_e the electron scattering angle and h the electron helicity. After applying corrections from the inclusive cases, the ratios have been compared to the results from MAID2007. The difference of the measured and MAID2007 model ratios for each pion paddle number is shown in Figure 1.12. One can conclude from Figure 1.12 that the "inclusive corrections" do not impact single pion production rates for the exclusive cases.

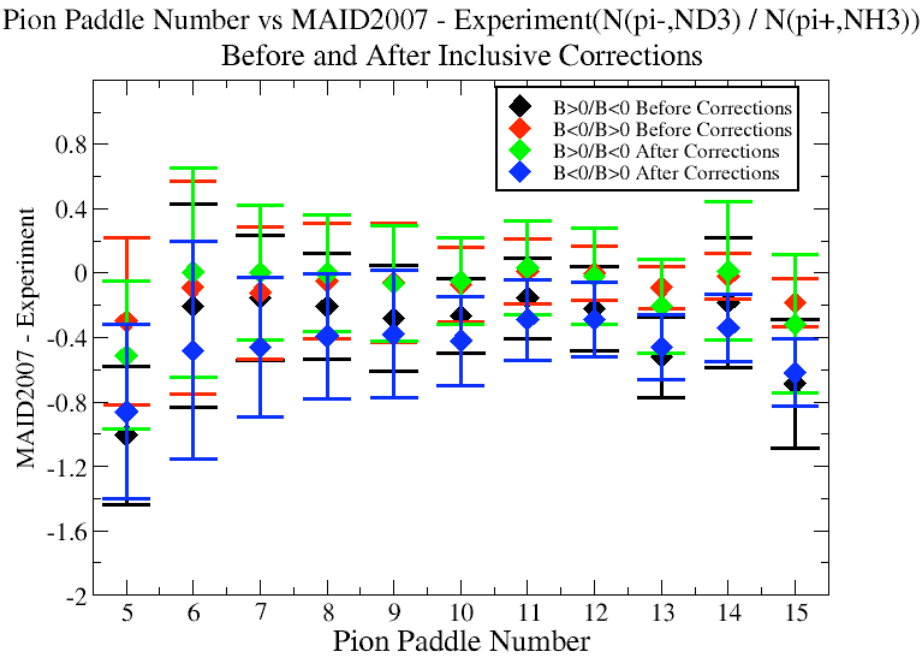

Fig. 1.12: Pion Paddle Number versus MAID2007 - Experiment(N(π^-,ND_3)/N(π^+,NH_3)). The Black and red data represent B>0/B<0 and B<0/B>0 cases respectively before corrections. The green and blue points represent the ratios for B>0/B<0 and B<0/B>0 after inclusive corrections.

1.3 Asymmetries

The double spin asymmetry measurements in this work are performed by comparing scattering events that occur when the incident probe spin and nuclear target spin are parallel to the scattering events that occur when the spins are anti-parallel.

1.3.1 Beam Charge Asymmetry

The helicity of the electron beam was flipped at a rate of 1 Hz. The helicity is prepared at the source such that helicity pairs are produced pseudo randomly.

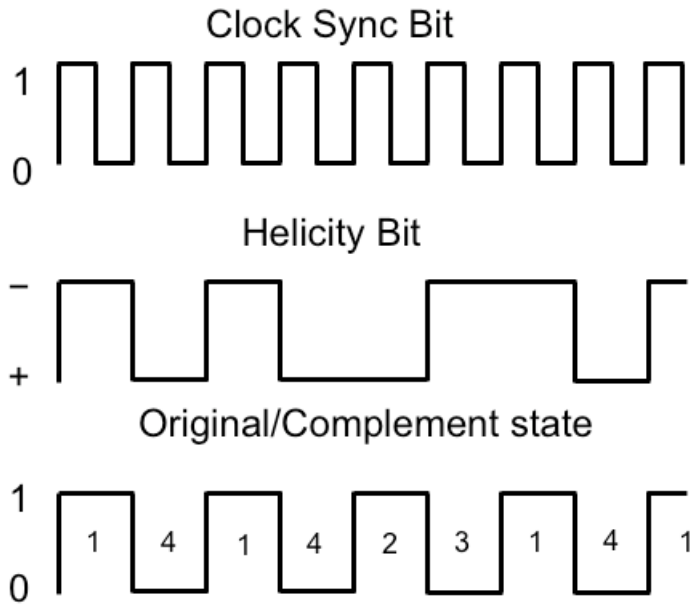

Fig. 1.13: The Helicity State: A one bit signal from the beam injector gives the helicity information, whereas a sync bit with a 2 Hz frequency is generated at the same time and is equal to the helicity flip time.

If the first electron bunch is pseudo randomly chosen to be positive (negative) then it is labeled as the original helicity state and denoted in software by a 2

(1). The next helicity state is prepared to be a complement to the first state and labeled in the software as either a 4, if the original helicity state was a 1 (negative), or 3 if the original helicity state was a 2 (positive). The helicity selection process is then repeated.

Figure 1.13 illustrates the signals used to label the helicity states. The clock pulse (SYNC) is used to indicate that a change in the pockel cell used to define the helicity state may have occurred. The helicity bit identifies the helicity state that was set. The original/complement pulse identifies if the state is an original or complement helicity state. All three bits are recorded in the raw data file for each event and then converted to the labels 1, 2, 3, 4 during DST file production once the particles have been reconstructed.

Two scalers were used to record several ancillary detectors, such as a Faraday cup and several PMTs mounted on the beam line, according to their helicity label. One of the scalers was gated by the DAQ live time in order to record beam conditions when the DAQ was able to take data and not busy recording data. The second scaler remained ungated. Both scalers recorded the SYNC and Helicity signals from the injector along with the counts observed from ancillary detectors during the SYNC interval. The Faraday cup signal recorded by the gated helicity scaler is used to normalize the events reconstructed during the same helicity interval. The beam charge asymmetry below is measured by the gated helicity scaler. For each run number, a gaussian fit was used to fit the beam charge asymmetry distributions as in Figure 1.14. The beam charge asymmetry is defined as

$$A_{BeamCharge} = \frac{\Sigma FC^{hel1,hel2} - \Sigma FC^{hel4,hel3}}{\Sigma FC^{hel1,hel2} + \Sigma FC^{hel4,hel3}}, \tag{1.21}$$

where $FC^{hel1,hel2}$ ($FC^{hel4,hel3}$) represents the Faraday cup counts observed for the original helicity 1 and 2 states (the complement helicity 3 and 4 states).

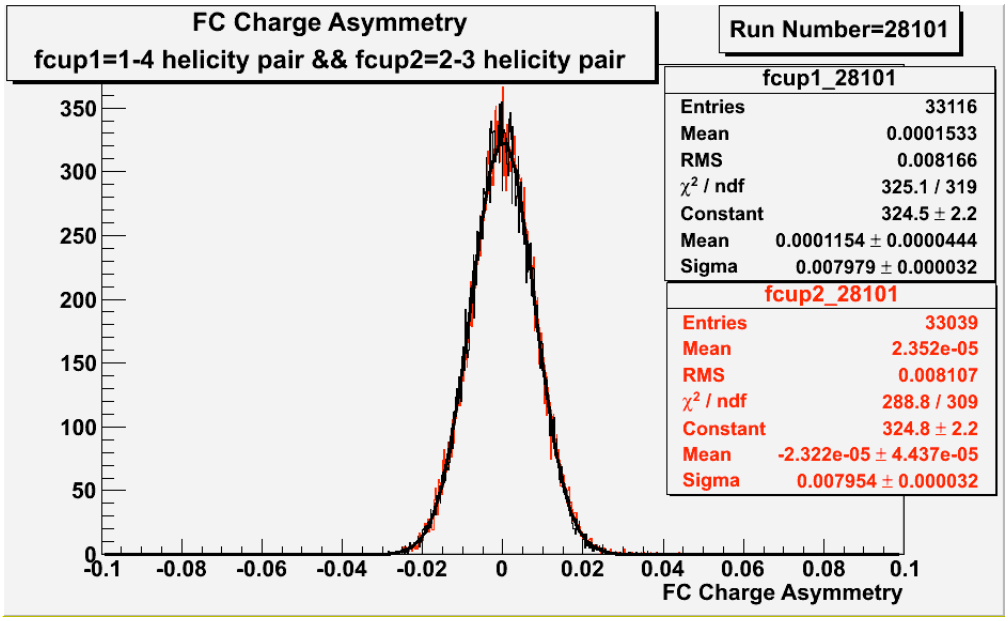

Fig. 1.14: Beam charge asymmetry for run #28101 using the gated Faraday cup counts for two helicity pairs (1-4 and 2-3 helicity pairs). $A_{1-4} = (11.5 \pm 4.4) \times 10^{-5}$ and $A_{2-3} = (-2.3 \pm 4.4) \times 10^{-5}$.

EG1b data sets, with the same half wave plane, target type, target polarization and beam torus, have been combined. The beam charge asymmetries have been calculated for the each run group and are listed in Table 1.2.

1.3.2 Electron Asymmetry

A measurement of the electron cross section helicity difference needs to account for a possible helicity dependence of the incident electron flux (charge Asymmetry). Figure 1.15 shows the reconstructed electron asymmetry before it is normalized by the gated Faraday Cup as a function of the run number for

Run Group	Half wave plane(HWP)	$A_{1-4} \times 10^{-4}$	$A_{2-3} \times 10^{-4}$
28100 – 28105	+1	5.88 ± 34.40	4.03 ± 34.36
28106 – 28115	-1	7.53 ± 22.30	8.28 ± 22.30
28145 – 28240	+1	31.70 ± 7.99	30.40 ± 7.99
28242 – 28284	-1	49.6 ± 10.8	47.9 ± 10.8
28286 – 28324	+1	36.3 ± 11.6	37.0 ± 11.5
28325 – 28447	-1	21.1 ± 13.4	22.2 ± 13.4
28449 – 28479	+1	-11.6 ± 16.5	-21.6 ± 16.5

Table 1.2: Run Group versus Beam Charge Asymmetry.

the 4.2 GeV data set. The reconstructed electron asymmetry can be defined following way:

$$A_{NES}^{+-} = \frac{NES^{+} - NES^{-}}{NES^{+} + NES^{-}} \equiv (2-3), \tag{1.22}$$

or

$$A_{NES}^{-+} = \frac{NES^{-} - NES^{+}}{NES^{-} + NES^{+}} \equiv (1-4), \tag{1.23}$$

where NES^{+} (NES^{-}) represents number of electron scattered for the positive (negative) beam helicity.

Systematic effects on the asymmetry measurement may be investigated by separating the data into two groups based on which helicity state is set first. The first group (black data points) represents the electron asymmetry observed when the first (original) helicity state is negative and its complement state is positive (helicity state #1 – state #4). The second group (red data points) represents the asymmetry observed when the first state is positive and the complement state is negative (helicity state #2 – #3). Both groups were divided into two subgroups based the target type used. The diamond points on the histogram represent the data for the NH_3 target and the squares for the ND_3 target.

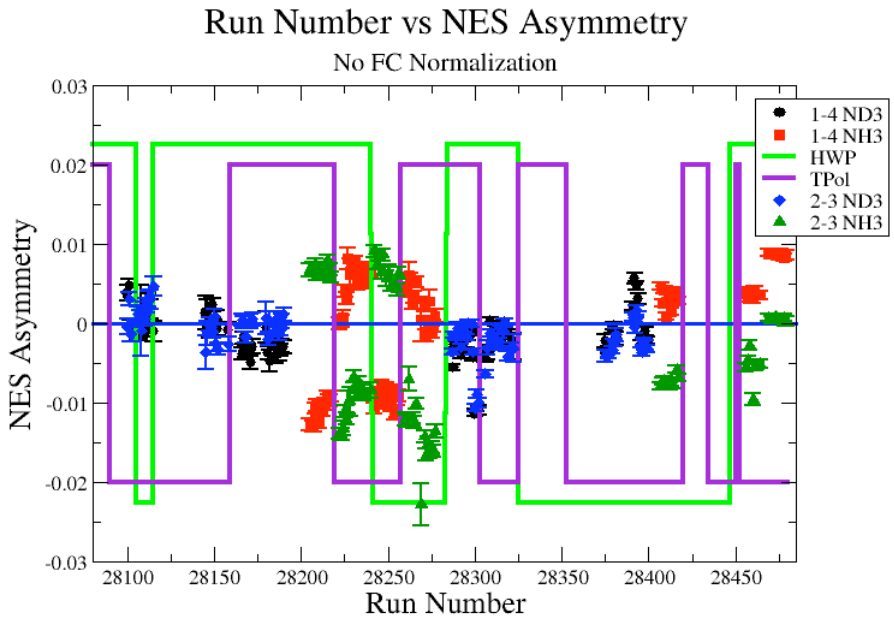

Fig. 1.15: Run Number versus Electron Asymmetry before FC normalization. The black and red points represent reconstructed electron asymmetry for the helicity 1-4 pair for ND_3 and NH_3 target respectively. The blue and green points represent the helicity pair 2-3 for ND_3 and NH_3 respectively. The green line shows the sign of the half wave plane (HWP) and the purple line is the sign of the target polarization (TPol).

Two lines on the histogram are used to identify the sign of the half wave plate (HWP) and the target polarization (TPol). The relative spin orientation can be changed by either inserting a half wave plane (HWP) or by populating a different target polarization state with a different RF frequency. One would expect the asymmetry to change sign if either the HWP is inserted or the target polarization is rotated 180 degrees. As one can see for Figure 1.16 and Figure 1.15, the electron asymmetry (sign(hel1-hel4), sign(hel3-hel2) and sign(hel42-hel13)) changes sign if the HWP or Target Polarization sign is changed.

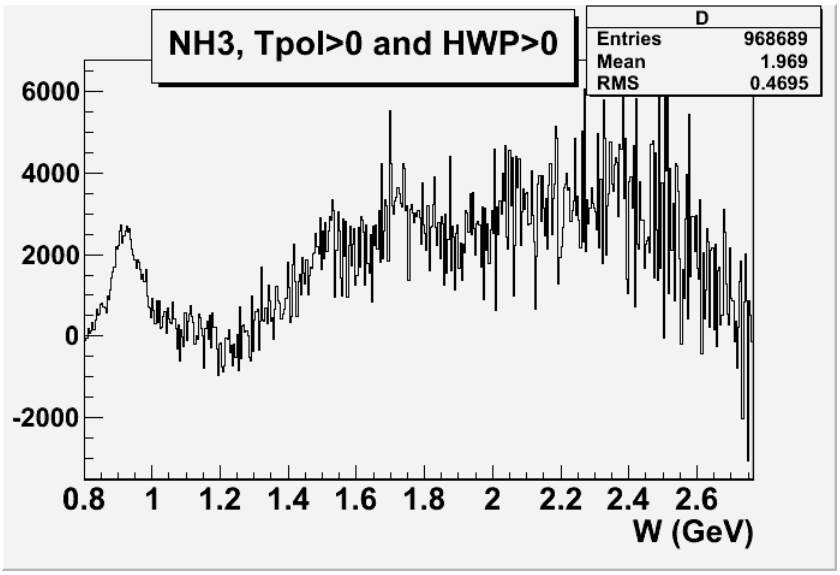

(a) NH3, Tpol>0 and HWP>0.

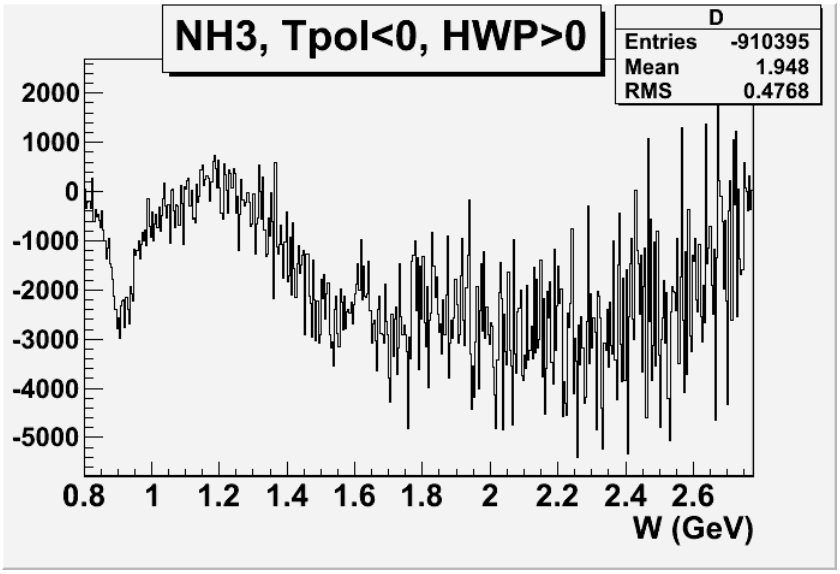

(b) NH3, Tpol<0 and HWP>0.

Fig. 1.16: W versus ($NES^{hel42} - NES^{hel13}$). The electron asymmetry (sign(hel42-hel13)) changes sign when the HWP or Target Polarization sign is changed.

The un-normalized reconstructed electron asymmetry has been calculated as:

$$A_{NES} = \frac{NES^{hel1,hel2} - NES^{hel4,hel3}}{NES^{hel1,hel2} + NES^{hel4,hel3}}, \tag{1.24}$$

and normalized by the Faraday cup

$$A_{NES}^{FCnormalized} = \frac{\frac{NES^{hel1,hel2}}{FC^{hel1,hel2}} - \frac{NES^{hel4,hel3}}{FC^{hel4,hel3}}}{\frac{NES^{hel1,hel2}}{FC^{hel1,hel2}} + \frac{NES^{hel4,hel3}}{FC^{hel4,hel3}}}. \tag{1.25}$$

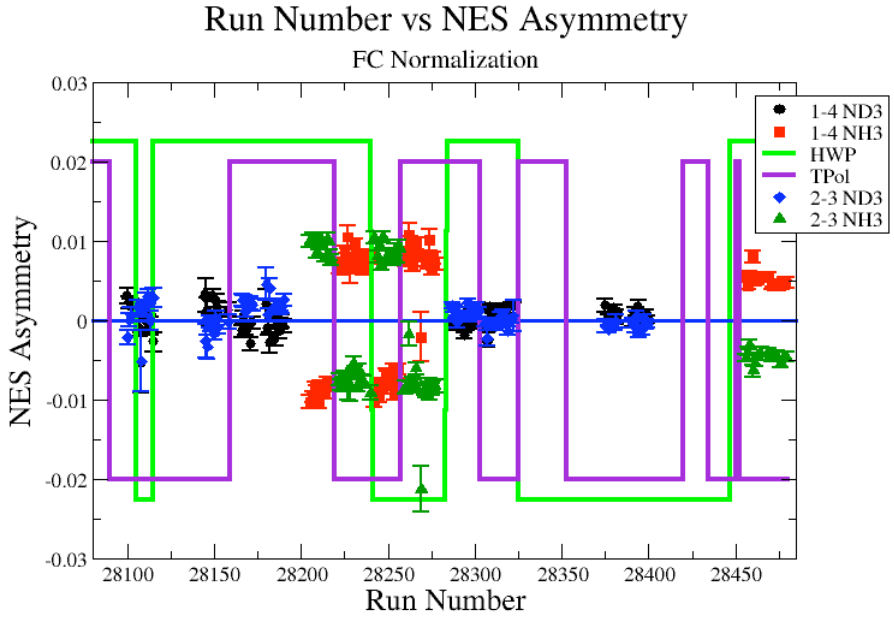

Fig. 1.17: Run Number versus Electron Asymmetry after applying FC normalization. The black and red points represent the reconstructed electron asymmetry for the helicity 1-4 pair for ND_3 and NH_3 target respectively. The blue and green points are the helicity pair 2-3 for ND_3 and NH_3 respectively. The green line shows the sign of the half wave plane (HWP) and the purple line is the sign of the target polarization (TPol).

1.3.3 Semi-Inclusive Asymmetries

The asymmetries from semi-inclusive pion electroproduction using proton or deuteron targets can be written in terms of the difference of the yield when the electron spin is parallel and antiparallel to the spin of the nucleon. There are four combinations of semi-inclusive asymmetries: $A^{\pi^+}_{NH_3}$, $A^{\pi^-}_{NH_3}$, $A^{\pi^+}_{ND_3}$ and $A^{\pi^-}_{ND_3}$

$$A^{\pi^+}_{NH_3} = \frac{N^{\uparrow\uparrow}_{NH_3,\pi^+} - N^{\uparrow\downarrow}_{NH_3,\pi^+}}{N^{\uparrow\uparrow}_{NH_3,\pi^+} + N^{\uparrow\downarrow}_{NH_3,\pi^+}} \tag{1.26}$$

$$A^{\pi^-}_{NH_3} = \frac{N^{\uparrow\uparrow}_{NH_3,\pi^-} - N^{\uparrow\downarrow}_{NH_3,\pi^-}}{N^{\uparrow\uparrow}_{NH_3,\pi^-} + N^{\uparrow\downarrow}_{NH_3,\pi^-}} \tag{1.27}$$

$$A^{\pi^+}_{ND_3} = \frac{N^{\uparrow\uparrow}_{ND_3,\pi^+} - N^{\uparrow\downarrow}_{ND_3,\pi^+}}{N^{\uparrow\uparrow}_{ND_3,\pi^+} + N^{\uparrow\downarrow}_{ND_3,\pi^+}} \tag{1.28}$$

$$A^{\pi^-}_{ND_3} = \frac{N^{\uparrow\uparrow}_{ND_3,\pi^-} - N^{\uparrow\downarrow}_{ND_3,\pi^-}}{N^{\uparrow\uparrow}_{ND_3,\pi^-} + N^{\uparrow\downarrow}_{ND_3,\pi^-}}, \tag{1.29}$$

where $N^{\uparrow\downarrow}_{NH_3,\pi^+,\pi^-}(N^{\uparrow\uparrow}_{NH_3,\pi^+,\pi^-})$ and $N^{\uparrow\downarrow}_{ND_3,\pi^+,\pi^-}(N^{\uparrow\uparrow}_{ND_3,\pi^+,\pi^-})$ represent the number of π^+ and π^- hadrons detected in the final state with the scattered electron, when the spin of the initial electron beam was antiparallel (parallel) to the spin of the proton and neutron respectively.

The kinematic coverage for the events used in the measured asymmetries are shown on Figure 1.18 and Figure 1.19. The semi-inclusive asymmetries are listed in Table 1.3. The first group $A_{hel1-hel4}$ represents the asymmetry measured when the first original electron spin (hel1) is antiparallel to the target nucleon spin and its complement state (hel4) is parallel, whereas the second group $A_{hel2-hel3}$ represents measuring the SIDIS asymmetry when the first he-

licity state is parallel (hel2) and its complement state is antiparallel to the spin of the nucleon. For the final measurement, the two groups are combined into one $A_{hel42-hel13}$ set. Instead of looking at original and complement electron helicity states, they have been combined into the positive (hel42) and negative (he13) helicity states, which are parallel and antiparallel to the spin of the target nucleon respectively.

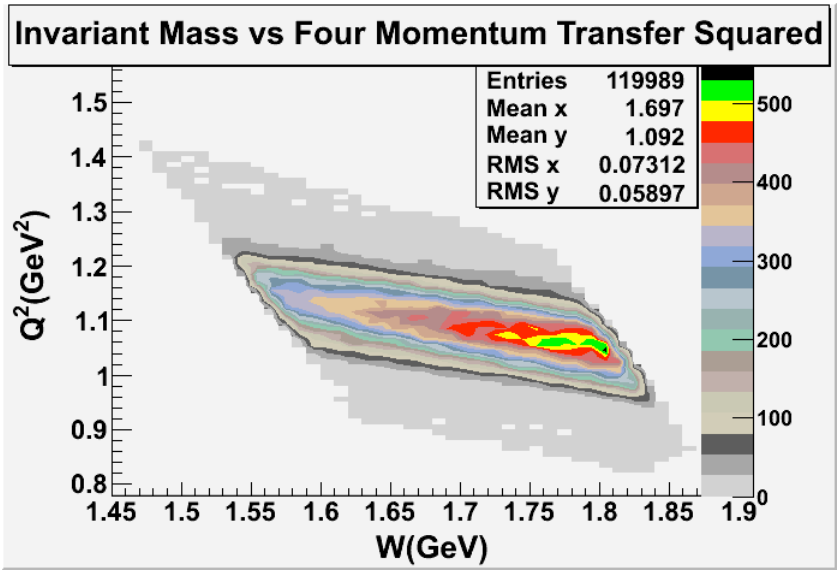

Fig. 1.18: Invariant Mass versus Q^2.

The ratio of the combined semi-inclusive deep inelastic asymmetries (A^{raw}) from Table 1.3, for two different torus settings have been corrected for the electron reconstruction efficiency. The Figure 1.20 represents the asymmetry ratios before and after electron reconstruction efficiency corrections. The ratios have been calculated for each target and charged pion type. The SIDIS asymmetries before and after the correction are statistically the same. The result indicates that the electron reconstruction efficiency does not change the asymmetries.

The data have been combined for each target type and asymmetries measured

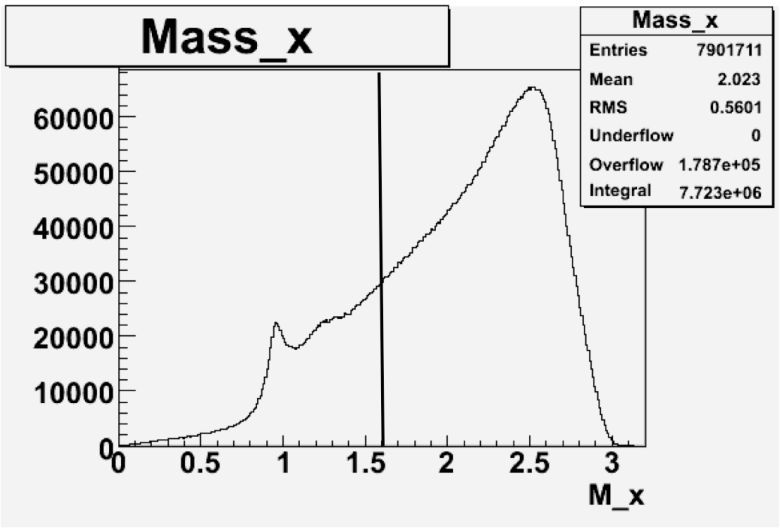

Fig. 1.19: Missing Mass.

Target type, Beam Torus	$A_{hel1-hel4} \times 10^{-4}$	$A_{hel2-hel3} \times 10^{-4}$	$A^{raw} \times 10^{-4}$
NH_3, B>0, π^+	-139.84 ± 81.52	143.15 ± 81.78	136.2 ± 57.74
NH_3, B<0, π^+	-223.76 ± 117.10	247.65 ± 116.59	237.69 ± 82.65
ND_3, B>0, π^-	-6.37 ± 188.73	-98.11 ± 188.03	9.21 ± 127.22
ND_3, B<0, π^-	-63.73 ± 105.14	-30.34 ± 6085.54	12.37 ± 71.10
NH_3, B>0, π^-	-155.45 ± 128.21	-72.55 ± 128.92	35.11 ± 90.91
NH_3, B<0, π^-	9.60 ± 119.31	72.94 ± 119.36	32.39 ± 84.38
ND_3, B>0, π^+	-76.59 ± 126.60	110.28 ± 126.13	92.25 ± 85.38
ND_3, B<0, π^+	-29.22 ± 107.53	123.98 ± 106.86	92.25 ± 85.38

Table 1.3: Run Number versus SIDIS Asymmetry for Each Type Target material and Beam Torus.

for two x_B values (Table 1.4). The SIDIS asymmetries were calculated for the following kinematic range: electron scattering angle $17.5 < \theta_e < 18.5$, electron momentum 2.55 GeV$<P_e<$2.75 GeV, invariant mass 1.6 GeV$<$W$<$1.8 GeV and momentum transferred squared 0.9 GeV$^2<Q^2<$1.3 GeV^2.

In addition to x_B, the data have been subdivided according to the fraction energy of the observed final state pion(z). $A_{NH_3}^{\pi^+,raw}$ asymmetries for two z are

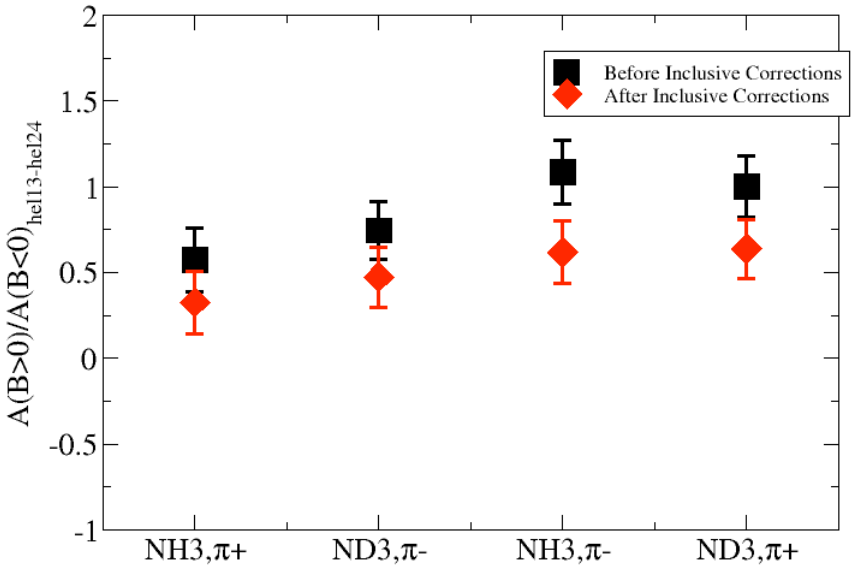

Fig. 1.20: The ratio of the SIDIS asymmetries for two torus field settings $\frac{A^{raw}(B>0)}{A^{raw}(B<0)}$ versus target and the charged pion type. The black squares represent the data before electron reconstruction efficiency and the red data - after electron reconstruction efficiency has been applied.

SIDIS Asymmetry	$x_B = 0.3$	$x_B = 0.4$
$A_{NH_3}^{\pi^+,raw}$	$(150.08 \pm 65.96) \times 10^{-4}$	$(217.20 \pm 69.06) \times 10^{-4}$
$A_{ND_3}^{\pi^-,raw}$	$(39.04 \pm 81.44) \times 10^{-4}$	$(91.90 \pm 96.14) \times 10^{-4}$
$A_{NH_3}^{\pi^-,raw}$	$(100.81 \pm 83.49) \times 10^{-4}$	$(-23.98 \pm 94.92) \times 10^{-4}$
$A_{ND_3}^{\pi^+,raw}$	$(53.17 \pm 74.89) \times 10^{-4}$	$(85.17 \pm 82.97) \times 10^{-4}$

Table 1.4: SIDIS Asymmetries for $x_B = 0.3$ and $x_B = 0.4$.

shown in Table 1.5.

z	$x_B = 0.3$	$x_B = 0.4$
0.4	$(125.62 \pm 81.92) \times 10^{-4}$	$(165.81 \pm 86.76) \times 10^{-4}$
0.7	$(140.32 \pm 158.98) \times 10^{-4}$	$(238.34 \pm 156.79) \times 10^{-4}$

Table 1.5: $A_{NH_3}^{\pi^+,raw}$ SIDIS Asymmetry.

1.3.4 Dilution Factor

To exclude the contributions of polarized nucleons from the non-hydrogen nuclei in the ammonia target (Nitrogen) and the cooling material of the target (Helium) cell to the semi-inclusive rates, the measured raw double spin asymmetries have to be divided by a dilution factor. The dilution factor accounts for the fraction of events coming from the desired polarized target nucleon. The dilution factors are calculated by combining the data from runs using different target types. During the EG1b experiment, several runs were taken with Carbon C^{12} and an empty target cell (He). All the runs in this work used liquid Helium as the coolant during the experiment. The Carbon and empty target runs were used to estimate the dilution of the data by the noise attributed to the interaction of the incident electron beam with the Nitrogen or Helium nucleons present in the target cell [8].

In order to calculate the dilution factor, we need to define the number of counts $N_{A,C,MT}^{hel13,hel24}$ with beam helicity negative and positive for ammonia, Carbon and empty target runs. All are weighted by the corresponding gated Faraday cup counts [9]. Normalized rates are defined as

$$n_{C,MT} = \frac{N_{C,MT}^{+} + N_{C,MT}^{-}}{FC^{+} + FC^{-}} \tag{1.30}$$

and

$$n_A = \frac{1}{2}(\frac{N_A^+}{FC^+} + \frac{N_A^-}{FC^-}), \tag{1.31}$$

where n_C is the rate from a Carbon target, n_{MT} is from an empty target and n_A is from one of the NH_3 or ND_3 ammonia targets.

The counts for all four targets (empty, Carbon and ammonia) can be expressed as the sum of counts from the entrance and exit window foils (ρ_F, l_F, σ_F), liquid Helium coolant (ρ_{He}, l_{He}, σ_{He}), Carbon(ρ_C, l_C, σ_C), Nitrogen (ρ_N, l_N, σ_N), Hydrogen (Deuterium) ($\rho_{H(D)}$, $l_{H(D)}$, $\sigma_{H(D)}$).

$$n_{MT} = \rho_F l_F \sigma_F + \rho_{He} L \sigma_{He} = f \rho_C l_C \sigma_C + \rho_{He} L \sigma_{He}, \tag{1.32}$$

$$n_C = \rho_F l_F \sigma_F + \rho_C l_C \sigma_C + \rho_{He}(L - l_C)\sigma_{He}, \tag{1.33}$$

and

$$n_A = \rho_F l_F \sigma_F + \rho He(L - l_A)\sigma_{He} + \rho_A l_A(\sigma_N + 3\sigma_{H(D)}), \tag{1.34}$$

where $f = \frac{\rho_F l_F \sigma_F}{\rho_C l_C \sigma_C}$, $\sigma_{H(D)}$ represents the Hydrogen (Deuteron) cross section.

Using above system of equations, we define two new spectra to account for the Carbon target and the difference in the amount of Helium in ammonia targets vice versa the Carbon target. For a target cell with length L and the Carbon target with length l_C, the Carbon and LHe contributions can be written

following way:

$$n'_{12C} = \frac{L}{L + fl_C} n_C - \frac{L - l_C}{L + fl_C} n_{MT} = \rho_C l_C \sigma_C \tag{1.35}$$

and

$$n'_{4He} = \frac{(1+f) l_{He}}{L + fl_C} n_{MT} - \frac{f l_{He}}{L + fl_C} n_C = \rho_{He} l_{He} \sigma_{He}, \tag{1.36}$$

where n'_{12C} is the rate from the Carbon nucleus only and n'_{He} is the rate from liquid Helium only. The length and densities are listed in Table 1.6.

We need to establish how the rate from the Carbon target is related to the rate from the N^{15} in NH_3 and ND_3. The cross section for N^{15} can be written in terms of the cross sections on C^{12} target material (σ_{12C}) and on a bound neutron in N^{15} (σ'_n).

$$\sigma_{15N} \approx \frac{7}{6}\sigma_{12C} + \sigma'_n = \left(\frac{7}{6} + \frac{\sigma'_n}{\sigma_{12C}}\right) \sigma_{12C}. \tag{1.37}$$

It is assumed that when the scattering occurs on protons inside the target material, the ratio of $\frac{\sigma'_n}{\sigma_{12C}} = 0$ and when the reaction happens on neutrons inside the target, the value of the ratio is $\frac{\sigma'_n}{\sigma_{12C}} = \frac{1}{6}$, because there are six bound neutrons in C^{12} [9].

Using above quantities the background represented by the number of counts due to the non-hydrogen and non-deuterium parts of the ammonia target can

be expressed as

$$\begin{aligned} n_B &= \left[\frac{\rho_A l_A}{\rho_C l_C}\left(\frac{7}{6}+\frac{\sigma'_n}{\sigma_{12C}}\right)+f\right] n'_{12C} + (L-l_A) n'_{4He} \\ &= n_{MT} + l_A\left[\frac{\rho_A}{\rho_C l_C}\left(\frac{7}{6}+\frac{\sigma'_n}{\sigma_{12C}}\right) n'_{12C} - n'_{4He}\right]. \end{aligned} \tag{1.38}$$

The dilution factor d_f is

$$d_f = \frac{n_A - n_B}{n_A}. \tag{1.39}$$

The dilution factor is compared below in Table 1.8:

Item	Description	Value
$\rho_F l_F$	Density times target length for empty target.	Al: 167 μm; 0.045 g/cm^2. Kapton: 384 μm; 0.055 g/cm^2. Total=Al + Kapton=0.0996 g/cm^2
$\rho_C l_C$	Density times target length for Carbon target.	0.498 g/cm^2
f	The ratio of counts from foils to the C^{12} slab in the Carbon target.	0.200
ρ_{He}	He density.	0.145 g/cm^3
L	The length of the target cell from the entrance to exit foil.	1.90 cm
ρ_C	C^{12} density.	2.17 g/cm^3
l_C	Carbon target length.	0.23 cm
ρ_{NH_3}	NH_3 density	0.917 g/cm^3
ρ_{ND_3}	ND_3 density	1.056 g/cm^3
l_A	Ammonia target length.	0.6 cm

Table 1.6: Length and density values for different types of target material reproduced from the EG1b experiment [9].

The fractional energy of the observed final state hadron(z)	Dilution Factor(d_f)
NH_3, π^+ && $z = 0.4$	0.160 ± 0.02
NH_3, π^+ && $z = 0.7$	0.152 ± 0.03

Table 1.7: Calculated dilution Factor for NH_3 target type.

Reaction	Dilution Factor(d_f)
Resonance region	0.11 - 0.13
Inclusive	0.14 - 0.17
Semi-Inclusive	0.122 - 0.182

Table 1.8: Dilution Factor compared with other results [8] [10].

1.3.5 Fragmentation $\Delta R_{np}^{\pi^+ + \pi^-}$

A test of fragmentation can be performed by calculating the ratio of the difference of polarized to unpolarized cross sections for proton and neutron targets $\Delta R_{np}^{\pi^+ + \pi^-}$ and showing that it is independent of z. The fragmentation function can be written following way

$$\begin{aligned} \Delta R_{np}^{\pi^+ + \pi^-}(x, z, Q^2) &= \frac{\Delta\sigma_p^{\pi^+ + \pi^-} - \Delta\sigma_n^{\pi^+ + \pi^-}}{\sigma_p^{\pi^+ + \pi^-} - \sigma_n^{\pi^+ + \pi^-}} \\ &= \frac{\Delta\sigma_p^{\pi^+ + \pi^-}}{\sigma_p^{\pi^+ + \pi^-} - \sigma_n^{\pi^+ + \pi^-}} - \frac{\Delta\sigma_n^{\pi^+ + \pi^-}}{\sigma_p^{\pi^+ + \pi^-} - \sigma_n^{\pi^+ + \pi^-}} \\ &= \frac{(\Delta u + \Delta\bar{u}) - (\Delta d + \Delta\bar{d})}{(u + \bar{u}) - (d + \bar{d})}(x, Q^2) \\ &= \frac{g_1^p - g_1^n}{F_1^p - F_1^n}(x, Q^2). \end{aligned} \tag{1.40}$$

The left side of the fragmentation function is calculated using the measured double spin asymmetries for the ammonia targets. However, the right side can

be extracted using the model.

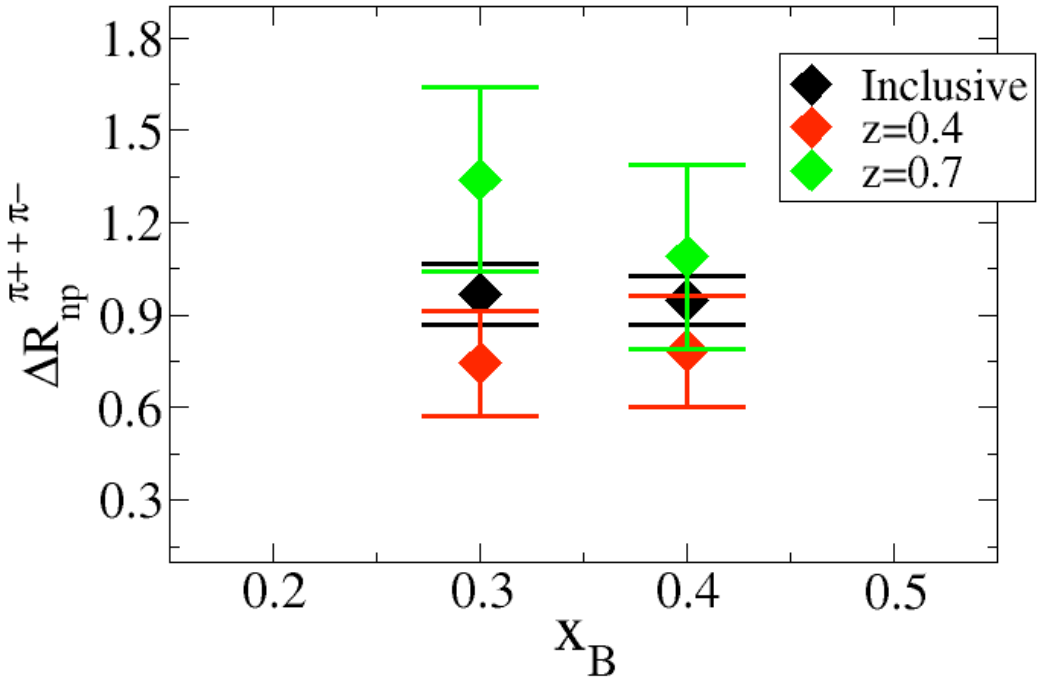

Fig. 1.21: x_B versus $\Delta R_{np}^{\pi^+ + \pi^-}$. Black data points represent the Model, red and green data points represent fragmentation function for $z = 0.4$ and $z = 0.7$ respectively.

z	$x_B = 0.3$	$x_B = 0.4$
0.4	14 %	12 %
0.7	21 %	32 %

Table 1.9: Statistical Z - test for the data comparison with the model. The probability of not observing the data point for each z and x_B values within the Inclusive Model.

The pion asymmetries, $A_{NH3}^{\pi^-}$, $A_{ND3^{\pi^+}}$, $A_{ND3}^{\pi^-}$ are statistically consistent with

zero as shown in Table 1.4. As a result, the contributions from $\Delta\sigma_p^{\pi^-}$, $\Delta\sigma_n^{\pi^+}$ and $\Delta\sigma_n^{\pi^-}$ to the fragmentation function test (Eq. 1.40) are negligible. Only the first term is non-zero in $\Delta R_{np}^{\pi^+ + \pi^-}$. After correcting the cross section difference for the target polarization, beam polarization, and dilution factor, the $\Delta R_{np}^{\pi^+ + \pi^-}$ function for two values of z and x_B is shown on Figure 1.21 and is compared to the Model.

1.3.6 Systematic errors

Systematic errors from the experimental setup and the cuts used for particle identification and background elimination were estimated. The systematic errors associated with the electromagnetic cuts and fiducial cuts for electron identification were calculated by comparing the SIDIS asymmetries before and after cuts were applied. Systematic effects related to the dilution factor and polarization were estimated following way: First, the SIDIS asymmetries were calculated for the standard values of the dilution factor and polarization. Then asymmetries were recalculated by changing the value of the each parameter by the amount of its uncertainty. The difference between these two values is the systematic effect. The systematic errors for the SIDIS asymmetries are shown in Table 1.10.

Source	Systematic Error
Geometrical and timing cuts	5.80×10^{-2}
Electromagnetic calorimeter cut	4.07×10^{-2}
Dilution Factor	5.03×10^{-2}
Target and beam polarization	1.10×10^{-2}
Total	8.76×10^{-2}

Table 1.10: The systematic errors for the $A_{NH_3}^{\pi^+}$ asymmetry.

Chapter 2

Results

The final results are presented in this section. They have been obtained by analyzing the data collected in 2000 - 2001 at Thomas Jefferson National Laboratory using a longitudinally polarized electron beam on a longitudinally polarized Hydrogen ($^{15}NH_3$) and Deuterium ($^{15}ND_3$) targets. The incident electron's energy was 4.2 GeV. The CEBAF Large Acceptance Spectrometer (CLAS) was used for particle detection. The measurements were made for the kinematic region where $x_B \geq 0.3$ and momentum transferred squared between 0.9 and 1.3 GeV^2. The SIDIS asymmetries were measured for four different values of x_B. The corrected measured semi-inclusive deep inelastic asymmetries $A^{\pi^+}_{NH3}$, $A^{\pi^-}_{NH3}$, $A^{\pi^+}_{ND3}$ and $A^{\pi^-}_{ND3}$ are shown below on Figures 2.1, 2.2, 2.3 and 2.4 respectively and compared to the asymmetries measured by the HERMES experiment. The measured SIDIS asymmetries on the proton and deuterium targets are in good agreement within their combined uncertainties. The SIDIS asymmetries for longitudinally polarized Hydrogen ($^{15}NH_3$) and Deuterium ($^{15}ND_3$) targets are listed in Table 2.1 for four values of x_B. The asymmetries have been corrected for the target and beam polarization [11] and dilution factor from ref[12].

x_B	$A^{\pi^+}_{NH3} \pm stat. \pm syst.$	$A^{\pi^-}_{NH3} \pm stat. \pm syst.$
0.30	$0.1644 \pm 0.0504 \pm 0.0753$	$0.1378 \pm 0.0745 \pm 0.0751$
0.35	$0.2733 \pm 0.0400 \pm 0.0764$	$0.1183 \pm 0.0583 \pm 0.0750$
0.40	$0.3308 \pm 0.0499 \pm 0.0772$	$-0.0917 \pm 0.0753 \pm 0.0749$
0.45	$0.2521 \pm 0.1257 \pm 0.0761$	$-0.1908 \pm 0.1942 \pm 0.0755$
x_B	$A^{\pi^+}_{ND3} \pm stat. \pm syst.$	$A^{\pi^-}_{ND3} \pm stat. \pm syst.$
0.30	$0.2273 \pm 0.0317 \pm 0.0809$	$0.1286 \pm 0.0320 \pm 0.0767$
0.35	$0.0209 \pm 0.0314 \pm 0.0747$	$0.1904 \pm 0.0319 \pm 0.0791$
0.40	$0.3368 \pm 0.0322 \pm 0.0877$	$0.1080 \pm 0.0330 \pm 0.0761$
0.45	$0.2408 \pm 0.0377 \pm 0.0816$	$0.5125 \pm 0.0392 \pm 0.1024$

Table 2.1: Semi-inclusive asymmetries on the proton and deuterium targets (A^{π^+,π^-}_{NH3} and A^{π^+,π^-}_{ND3}).

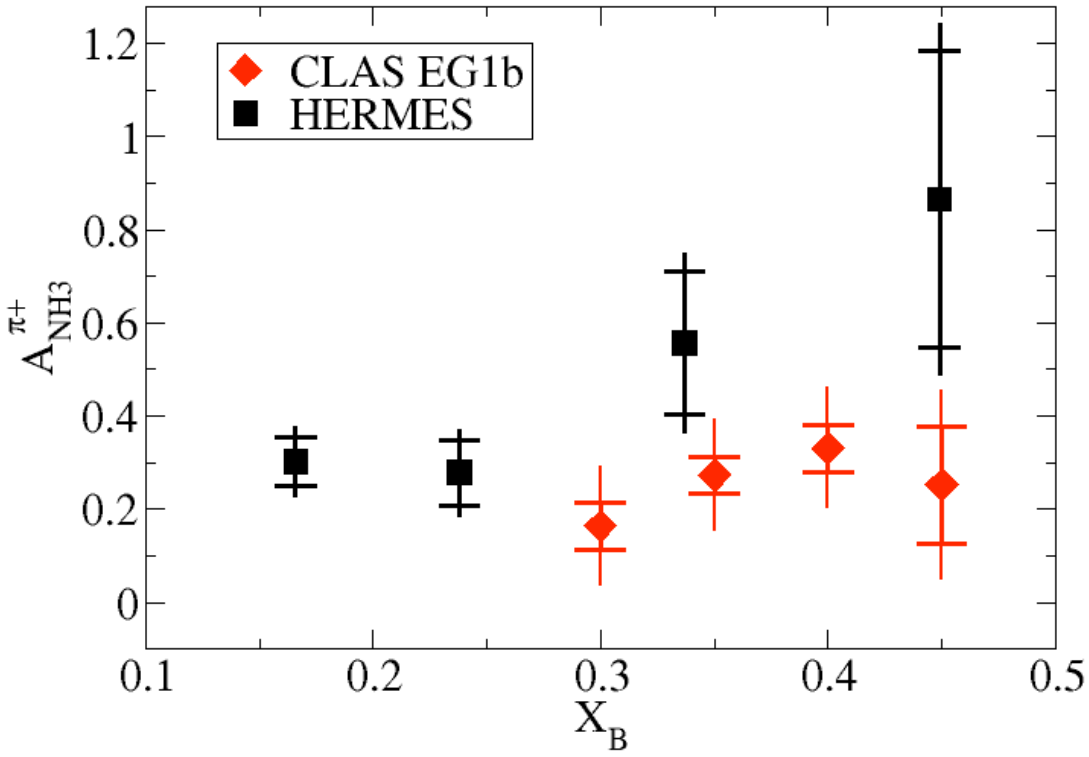

Fig. 2.1: x_B versus $A_{NH3}^{\pi^+}$ SIDIS Asymmetry. The solid black squares are measurements from ref[13] and the solid red diamonds represent SIDIS asymmetries measured using the data collected during the EG1b experiment. The error bar lines represent systematic uncertainty and the risers statistical uncertainty.

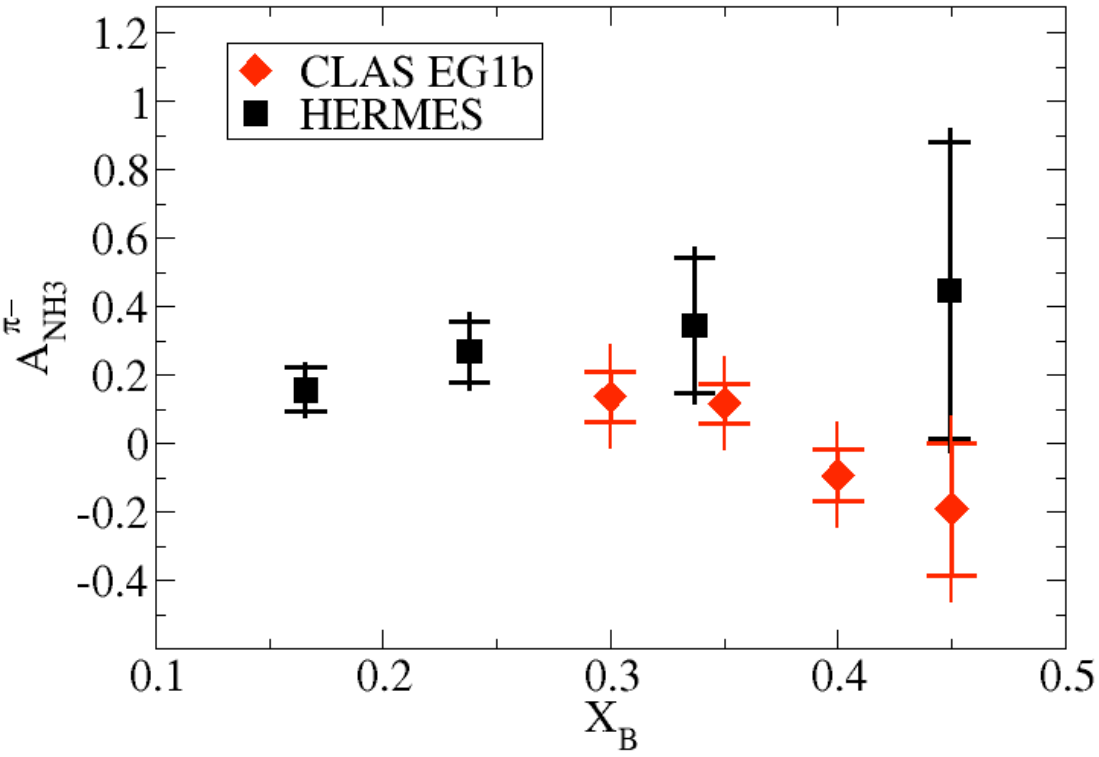

Fig. 2.2: x_B versus $A_{NH3}^{\pi^-}$ SIDIS Asymmetry. The solid black squares are measurements from ref[13] and the solid red diamonds represent SIDIS asymmetries measured using the data collected during the EG1b experiment. The error bar lines represent systematic uncertainty and the risers statistical uncertainty.

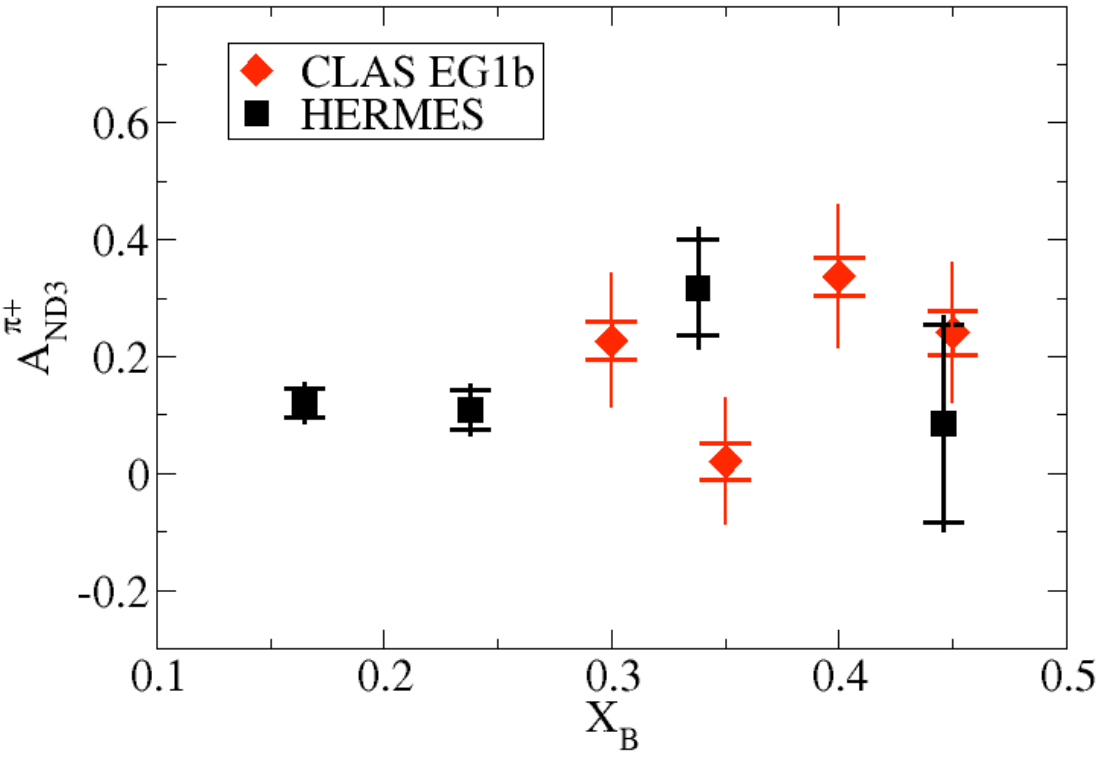

Fig. 2.3: x_B versus $A_{ND3}^{\pi^+}$ SIDIS Asymmetry. The solid black squares are measurements from ref[13] and the solid red diamonds represent SIDIS asymmetries measured using the data collected during the EG1b experiment. The error bar lines represent systematic uncertainty and the risers statistical uncertainty.

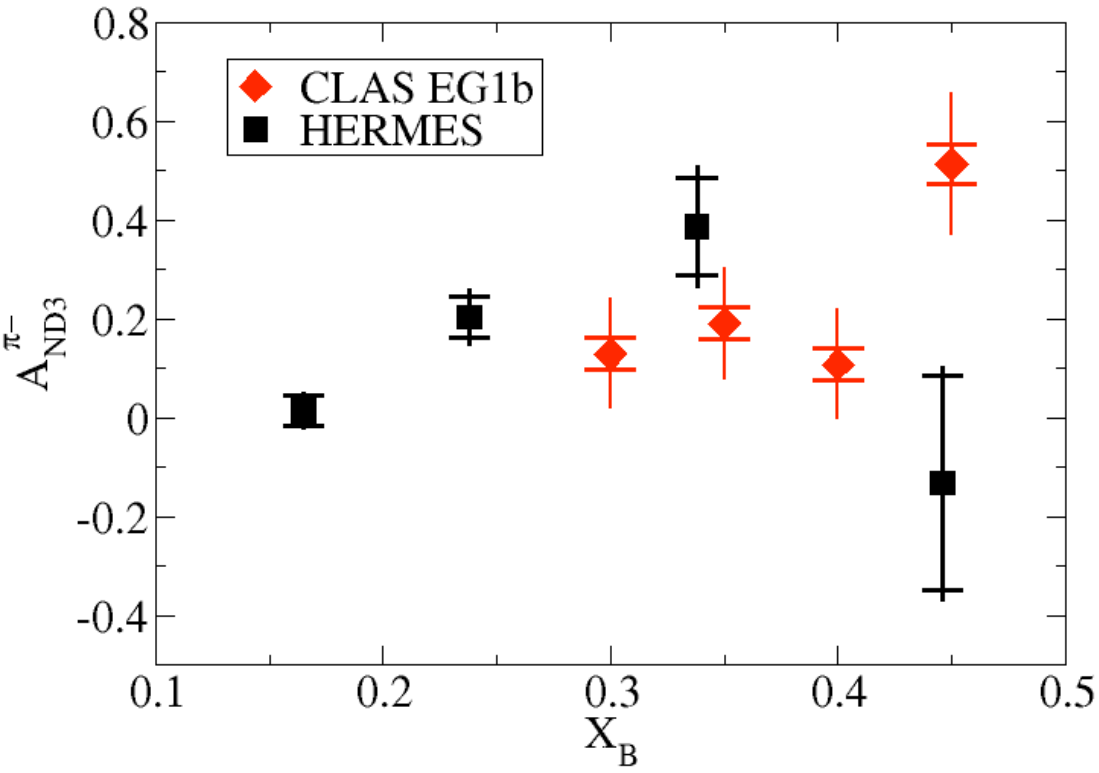

Fig. 2.4: x_B versus $A^{\pi^-}_{ND3}$ SIDIS Asymmetry. The solid black squares are measurements from ref[13] and the solid red diamonds represent SIDIS asymmetries measured using the data collected during the EG1b experiment. The error bar lines represent systematic uncertainty and the risers statistical uncertainty.

Bibliography

[1] E. Christova and E. Leader, *Semi-inclusive production-tests for independent fragmentation and for polarized quark densities*. hep-ph/9907265 (1999).

[2] K. Nakamure *et. al.*, The Review of Particle Physics. Particle Data Group. J. Phys. G **37**, 075021 (2010).

[3] M. Osipenko, A. Vlassov and M. Taiuti, *Matching between the electron candidate track and the Cherenkov counter hit*. CLAS-NOTE 2004-020 (2004).

[4] C. Lanczos, SIAM Journal of Numerical Analysis, B**1**, 86 (1964).

[5] K. Park, V. D. Burkert and W. Kim (The CLAS Collaboration), Phys. Rev. C**77**, 015208 (2008).

[6] J. Pierce, *Pion Identification code*,
From EG1 Hall-B, WWW Document,
(http://www.jlab.org/Hall-B/secure/eg1/EG2000/josh/pion.cc).

[7] Unitary Isobar Model, MAID2007, WWW Document,
(http://wwwkph.kph.uni-mainz.de/MAID//maid2007/maid2007.html).

[8] R. G. Fersch, *Measurement of Inclusive Proton Double Spin Asymmetries and polarized Structure Functions*. Doctoral dissertation. The College of William and Mary, Williamsburg, VA (2008).

[9] S. E. Khun, *Dilution Factor for Exclusive Channels*. Old Dominion University, Norfolk, VA (2010).

[10] Y. A. Prok, *Measurement of The Spin Structure Function $g_1(x, Q^2)$ of the Proton in The Resonance Region*. Doctoral dissertation. University of Virginia, Richmond, VA, 2004.

[11] K. V. Dharmawardane *et. al.*, (The CLAS Collaboration), Phys. Lett. **B641**, 11 (2006).

[12] P. Bosted *et. al.*, *Interpolated model calculated dilution factors for EG1b directly from radiated cross-sections*, WWW Document, (http://www.jlab.org/Hall-B/secure/eg1/EG2000/fersch/DILUTION/dilutionmodel/) (2007).

[13] A. Airapetian *et. al.*, (The HERMES Collaboration), Phys. Rev. Lett. 92, 012005 (2004).